# Magnetoplasmon excitations in arrays of circular and noncircular quantum dots

B. P. van Zyl and E. Zaremba
*Department of Physics, Queen's University, Kingston, Ontario, Canada K7L 3N6*

D. A. W. Hutchinson
*Clarendon Laboratory, Parks Road, University of Oxford, Oxford, England*
(Received 17 August 1999)

We have investigated the magnetoplasmon excitations in arrays of circular and noncircular quantum dots within the Thomas-Fermi-Dirac-von Weizsäcker approximation. Deviations from the ideal collective excitations of isolated parabolically confined electrons arise from local perturbations of the confining potential as well as interdot Coulomb interactions. The latter are unimportant unless the interdot separations are of the order of the size of the dots. Local perturbations such as radial anharmonicity and noncircular symmetry lead to clear signatures of the violation of the generalized Kohn theorem. In particular, the reduction of the local symmetry from $SO(2)$ to $C_4$ results in a resonant coupling of different modes and an observable anticrossing behavior in the power absorption spectrum. Our results are in good agreement with recent far-infrared transmission experiments.

## I. INTRODUCTION

Advances in nanofabrication technology have opened up the possibility of studying electronic systems under a wide range of confinement conditions. The systems of interest are usually fabricated by starting with a two-dimensional electron gas and applying various lateral modulation techniques.[1–3] In this way, systems such as wires, dots, rings, and antidot arrays have been realized. A powerful method for studying these systems is far-infrared (FIR) absorption spectroscopy. The observation of collective plasmon excitations and their dispersion in an applied magnetic field can yield a great deal of information about the effects of electron-electron interactions and the influence of different forms of geometrical confinement.

In this paper, we are primarily interested in the magnetoplasmon excitations in quantum dot arrays. In particular, we focus on the experimental results of Demel *et al.*[4,5] which reveal interesting features in the absorption spectrum as a function of magnetic field. It is by now well understood that the observed deviations from the ideal spectrum expected for parabolic confinement[6–8] are mainly due to anharmonic perturbations of the confining potential.[9–12] For parabolic confinement, the only allowed dipole excitations correspond to center of mass motion and have the frequencies $\omega_\pm = \sqrt{\omega_0^2+(\omega_c/2)^2} \pm \omega_c/2$, where $\omega_0$ is the harmonic confining frequency and $\omega_c$ is the cyclotron frequency. In a previous paper[12] it was shown that an axially symmetric $r^4$ perturbation leads to a coupling of the center-of-mass mode to other dipole excitations of the harmonic potential, and gives rise to a satellite peak, which tracks along the $\omega_+$ excitation. The calculated absorption spectrum was found to be in good agreement with experiment with regard to both the position and strength of the satellite peak.

One feature, which this earlier calculation[12] did not account for was an anticrossing behavior observed at lower magnetic fields. It was originally conjectured[4,5] that this feature was due to the nonlocal dynamic response associated with the finite compressibility of an electron gas and responsible for the wave-vector dispersion of plasmons in a uniform system. An explanation on the basis of a noncircular confining potential was dismissed on the grounds that the observed anticrossing did not conform with its expected dependence on $N$, the number of electrons in the dot. Subsequent work, however, shifted towards the noncircular confining potential as being the most likely explanation of the observed behavior. Gudmundsson and Gerhardts[9] performed random-phase approximation calculations for a parabolic dot with $10 \leqslant N \leqslant 30$ and argued, on the basis of the coupling between the center of mass and relative degrees of freedom induced by an $x^2y^2$ perturbation, that an anticrossing of the dipole mode with modes of higher multipolarity is to be expected. Pfannkuche and Gerhardts[10] arrived at similar conclusions based on an exact diagonalization of the dot Hamiltonian with quartic perturbations, but only for $N=2$. A classical electrostatic model was used by Nazin *et al.*[11] to study the magnetoplasmon modes in a parabolic dot with an $r^4\cos(4\theta)$ perturbation. This approach, which treats the electrons as a charged classical fluid, can be formulated in terms of an approximate energy functional that includes only the effects of the confining potential and the electrostatic repulsion between the electrons. The model is useful for large $N$ and was shown to provide a good description of the dynamics in anharmonic dots.[12] However, the theory proved to be ill defined for noncircular dots as a result of the singular behavior of the equilibrium density at the edge of the dot,[11] and a rigorous analysis of the dynamics could not be provided.

Our purpose here is to re-examine circular and noncircular quantum dots within the Thomas-Fermi-Dirac-von Weizsäcker (TFDW) hydrodynamic theory developed in the context of parabolically confined electron slabs.[13] The theory was later applied to electron rings[14] and was shown to give a good account of the edge magnetoplasmon modes observed in this system. The theory improves on the classical electrostatic model in that the quantum kinetic energy is included at

 

the level of the TFDW approximation. In addition, exchange-correlation effects can also be included. Unlike other hydrodynamic-based models,[15–19] the TFDW hydrodynamic theory incorporates the calculated equilibrium properties of the electronic density and thereby provides a more physical description of the collective modes.

The approach that we use is best suited to treating the FIR response of dots with a large number of electrons where the response is expected to be dominated by collective-like excitations. For few electrons, the underlying electronic structure can play an important role. In this situation, methods based on the random phase approximation are more appropriate, and calculations for noncircular dots in this regime have recently appeared.[20,21] However, these calculations cannot be extended readily to dots with a large number of electrons, which is the regime of interest in this paper.

Our paper is organized as follows. In Sec. II, we present an overview of the TFDW formalism and develop the constitutive equations for the theory in the context of a bidirectionally modulated electronic system. In Sec. III, we apply our theory to dot arrays and examine the effects of confinement symmetry and interdot coupling on the magnetoplasmon modes of the system. Finally, in Sec. IV, we present our concluding remarks. A brief account of this work will appear as a conference proceeding.[22]

## II. THE TFDW FORMALISM

The equilibrium and hydrodynamic properties of a periodically modulated two-dimensional electron gas (2DEG) within the TFDW approximation have already been discussed at some length in our previous work on uniaxially modulated electronic systems.[23] In this section, we provide an overview of the TFDW formalism and extend our earlier work to the more general case of bidirectional modulation. Since these calculations parallel those in Ref. 23, we only present the essential ingredients of the model here and refer to our earlier papers for details.[13,23]

### A. Equilibrium properties

As in all density-functional theory schemes,[24] the equilibrium properties of the system are obtained by finding the variational minimum of an energy functional. In atomic units ($e^2/\epsilon = m^\star = \hbar = 1$), the TFDW functional is given by

$$E[n] = \int d^2\mathbf{r}\left[\frac{\pi}{2}n^2 + \frac{\lambda_w}{8}\frac{|\nabla n(\mathbf{r})|^2}{n(\mathbf{r})} - \frac{4}{3}\sqrt{\frac{2}{\pi}}n^{3/2}\right] + \frac{1}{2}\int d^2\mathbf{r}\int d^2\mathbf{r}'\frac{n(\mathbf{r})n(\mathbf{r}')}{|\mathbf{r}-\mathbf{r}'|} + \int d^2\mathbf{r}\; v_{\rm ext}(\mathbf{r})n(\mathbf{r}). \tag{1}$$

The first term in Eq. (1) is the Thomas-Fermi kinetic energy, the second term is a von Weizsäcker-like correction to the kinetic energy,[25] and the third term is the Dirac local exchange energy. For simplicity, we neglect any correlation contribution. Following our earlier work,[23] we choose a value of $\lambda_w = 0.25$ for the von Weizsäcker coefficient. Our results are not strongly dependent on this value since the systems studied are primarily in the Thomas-Fermi regime.

A variation of Eq. (1) with respect to the density leads to the Euler-Lagrange equation

$$\frac{\delta E[n]}{\delta n(\mathbf{r})} - \mu = 0, \tag{2}$$

where the Lagrange multiplier $\mu$ (chemical potential) serves to fix the total number of electrons $N$. Introducing the so-called von Weiszäcker wave function, $\psi(\mathbf{r}) \equiv \sqrt{n(\mathbf{r})}$, into Eq. (2) we obtain

$$-\frac{\lambda_w}{2}\nabla^2\psi(\mathbf{r}) + v_{\rm eff}(\mathbf{r})\psi(\mathbf{r}) = \mu\psi(\mathbf{r}), \tag{3}$$

where the effective potential is given by

$$v_{\rm eff}(\mathbf{r}) = \pi\psi^2(\mathbf{r}) - \sqrt{\frac{8}{\pi}}\psi(\mathbf{r}) + \phi(\mathbf{r}) + v_{\rm ext}(\mathbf{r}). \tag{4}$$

Here, $\phi(\mathbf{r}) = \int d\mathbf{r}'\, n(\mathbf{r}')/|\mathbf{r}-\mathbf{r}'|$ is the electrostatic potential arising from the electronic density $n(\mathbf{r})$, and $v_{\rm ext}(\mathbf{r})$ is the externally imposed potential. The latter is assumed to be periodic with periodicities $a_x$ and $a_y$ in the $x$ and $y$ directions, respectively, and to have inversion symmetry about the center of the unit cell.

Equations (3) and (4) are reminiscent of the usual Kohn-Sham equations except that only a single electronic orbital need be calculated. It should also be noted that the effective potential $v_{\rm eff}$ includes a term coming from the Thomas-Fermi kinetic energy which does not appear in the usual Kohn-Sham potential. The required solution to Eq. (3) is the ground state von Weiszäcker wave function, $\psi_0$, which is obtained by imposing the boundary condition

$$\hat{\mathbf{n}}\cdot\nabla\psi_0 = \mathbf{0}, \tag{5}$$

at the edges of the unit cell. Here, $\hat{\mathbf{n}}$ is a unit normal vector. To complete the specification of $\psi_0$ we must also impose the normalization

$$\int d^2\mathbf{r}\, n_0(\mathbf{r}) = N, \tag{6}$$

which fixes the chemical potential $\mu$.

The self-consistent solution of Eqs. (3) and (4) can be obtained by direct iteration,[23] but care must be taken to avoid numerical instabilities associated with charge fluctuations. Here we adopt an alternative method to avoid this difficulty. We use the method of imaginary time evolution defined by the equation

$$\dot{\psi} = -(H-\mu)\psi, \tag{7}$$

where $H$ is the TFDW Hamiltonian given by

$$H = -\frac{\lambda_w}{2}\nabla^2 + v_{\rm eff}. \tag{8}$$

Using a first-order approximation for the time derivative on the left hand side of Eq. (7), we have

$$\psi(t+\delta t) = \psi(t) + (\mu - H)\psi(t)\,\delta t, \tag{9}$$

where $\mu$ is given by

$$\mu \simeq \frac{\int d\mathbf{r}\, \psi^* H \psi}{\int d\mathbf{r}\, \psi^* \psi}. \tag{10}$$

Once an initial guess for $\psi(t=0)$ has been made, Eq. (9) provides an updated $\psi(t)$ which is used in the next iteration to determine an updated $H$ and $\mu$, and so on until convergence. This scheme preserves the normalization of the wave function to $O(\delta t^2)$, but the wave function is nonetheless normalized to unity at each iteration. A combination of real-space and Fourier-space representations is used to evaluate the effect of $H$ on $\psi$. We have found this method of generating $\psi_0$ to be very stable against the charge fluctuation induced Coulomb instability.

### B. Hydrodynamic equations

A theory for the collective excitations of a modulated 2DEG is constructed by treating the electronic system as an inviscid, charged ''classical'' fluid. In particular, we adopt the hydrodynamic equations[13,23]

$$\left(\frac{\partial n}{\partial t}\right) + \nabla \cdot (n\mathbf{v}) = 0, \tag{11}$$

and

$$n\left[\frac{\partial \mathbf{v}}{\partial t} + \mathbf{v}\cdot\nabla\mathbf{v}\right] = n\mathbf{F}^{\rm tot}, \tag{12}$$

where the total force acting on a fluid element, $\mathbf{F}^{\rm tot} = \mathbf{F}^{\rm int} + \mathbf{F}^{\rm ext}$, consists of the internal force

$$\mathbf{F}^{\rm int}(\mathbf{r},t) = -\nabla\left[v_{\rm eff}(\mathbf{r},t) - \frac{\lambda_w}{2}\frac{\nabla^2\psi(\mathbf{r},t)}{\psi(\mathbf{r},t)}\right], \tag{13}$$

and the force due to external electromagnetic fields ($c=1$)

$$\mathbf{F}^{\rm ext} = -(\mathbf{E}^{\rm ext} + \mathbf{v}\times\mathbf{B}^{\rm ext}). \tag{14}$$

We wish to show here that these hydrodynamic equations can be obtained within a Lagrangian formulation. We suppose that the external electromagnetic field is defined in terms of a scalar potential $\phi^{\rm ext}$ and a vector potential $\mathbf{A}^{\rm ext}$ by

$$\mathbf{E}^{\rm ext} = -\nabla\phi^{\rm ext} - \frac{\partial \mathbf{A}^{\rm ext}}{\partial t}, \quad \mathbf{B}^{\rm ext} = \nabla\times\mathbf{A}^{\rm ext}, \tag{15}$$

and that the velocity field $\mathbf{v}(\mathbf{r},t)$ is defined by

$$\mathbf{v}(\mathbf{r},t) = \nabla g_1(\mathbf{r},t) + g_2(\mathbf{r},t)\nabla g_3(\mathbf{r},t) + \mathbf{A}^{\rm ext}. \tag{16}$$

Here, the $g_i$'s are three independent scalar functions; $g_1$ is associated with the irrotational part of the fluid flow and $g_2$ and $g_3$ are introduced to represent the solenoidal part. The dependence on the vector potential is displayed as a separate term.

The Lagrangian density that we propose is given by

$$\mathcal{L} = n\left(\frac{\mathbf{v}^2}{2} + \frac{\partial g_1}{\partial t} + g_2\frac{\partial g_3}{\partial t}\right) - n\phi^{\rm ext} + \varepsilon[n], \tag{17}$$

where $\varepsilon[n]$ is the TFDW energy density. Application of the principle of least action

$$\delta\int dt \int d\mathbf{r}\, \mathcal{L} = 0, \tag{18}$$

for each of the variables $\{g_1, g_2, g_3, n\}$ generates four equations. It is straightforward to show that independent variations of the $g_i$ yield the following equations:

$$\frac{\partial n}{\partial t} + \nabla\cdot(n\mathbf{v}) = 0, \tag{19}$$

$$\frac{\partial g_2}{\partial t} + \mathbf{v}\cdot\nabla g_2 = 0, \tag{20}$$

$$\frac{\partial g_3}{\partial t} + \mathbf{v}\cdot\nabla g_3 = 0. \tag{21}$$

Equation (19) is just the expected continuity equation.

Now, a variation of Eq. (18) with respect to $n$ yields

$$\left(\frac{\mathbf{v}^2}{2} + \frac{\partial g_1}{\partial t} + g_2\frac{\partial g_3}{\partial t}\right) - \phi^{\rm ext} + \left(v_{\rm eff} - \frac{\lambda_w}{2}\frac{\nabla^2\psi}{\psi}\right) = 0. \tag{22}$$

Taking the gradient of Eq. (22), along with the time differentiated form of Eq. (16), we obtain

$$\frac{\partial \mathbf{v}}{\partial t} + (\mathbf{v}\cdot\nabla)\mathbf{v} + \mathbf{E}^{\rm ext} + \mathbf{v}\times(\nabla\times\mathbf{v}) - \frac{\partial g_2}{\partial t}\nabla g_3 + \frac{\partial g_3}{\partial t}\nabla g_2 + \nabla\left(v_{\rm eff} - \frac{\lambda_w}{2}\frac{\nabla^2\psi}{\psi}\right) = 0. \tag{23}$$

Using Eq. (16) to evaluate the triple cross product, we have

$$\mathbf{v}\times(\nabla\times\mathbf{v}) = (\mathbf{v}\cdot\nabla g_3)\nabla g_2 - (\mathbf{v}\cdot\nabla g_2)\nabla g_3 + \mathbf{v}\times\mathbf{B}^{\rm ext}, \tag{24}$$

and substituting this result together with Eqs. (20) and (21) into Eq. (23), we finally obtain

$$\frac{\partial \mathbf{v}}{\partial t} + \mathbf{v}\cdot\nabla\mathbf{v} = -\nabla\left(v_{\rm eff} - \frac{\lambda_w}{2}\frac{\nabla^2\psi}{\psi}\right) - (\mathbf{E}^{\rm ext} + \mathbf{v}\times\mathbf{B}^{\rm ext}). \tag{25}$$

Equations (19) and (25) are equivalent to the two Eqs. (11) and (12) written down at the beginning of this section. These are the fundamental hydrodynamic equations of the TFDW theory.

Linearizing our hydrodynamic equations about small deviations from equilibrium, viz., $n(\mathbf{r},t) \to n_0 + \delta n(\mathbf{r},t)$, and retaining only first-order quantities, Eqs. (11) and (12) yield

$$\frac{\partial \delta n}{\partial t} + \nabla\cdot(n_0\mathbf{v}) = 0, \tag{26}$$

and

$$\frac{\partial \mathbf{v}}{\partial t} = \delta\mathbf{F}^{\rm int} - \mathbf{E}^{\rm ext} - \mathbf{v}\times\mathbf{B}^{\rm ext}, \tag{27}$$

where the fluctuating force is given by

$$\delta\mathbf{F}^{\rm int}(\mathbf{r},t) = -\nabla\left[\delta v_{\rm eff}(\mathbf{r},t) - \frac{\lambda_w}{2\psi_0}\nabla^2\delta\psi(\mathbf{r},t) + \frac{\lambda_w}{2}\frac{\nabla^2\psi_0}{\psi_0^2}\delta\psi(\mathbf{r},t)\right] \equiv -\nabla f, \tag{28}$$

with

$$\delta v_{\rm eff}(\mathbf{r},t) = 2\pi\psi_0\delta\psi(\mathbf{r},t) - \sqrt{\frac{8}{\pi}}\delta\psi(\mathbf{r},t) + \delta\phi(\mathbf{r},t). \tag{29}$$

The quantity $f$ plays the role of an effective potential for the internal force fluctuation. The magnetic field $\mathbf{B}^{\rm ext}$ will be taken to be a uniform field in the $z$ direction.

For the moment, we shall consider the normal modes of the system, which are determined in the absence of the driving field $\mathbf{E}^{\rm ext}$. Combining Eqs. (26) and (27) leads to the following equation for the fluctuating part of the von Weizsäcker wave function ($\delta\psi = \delta n/2\psi_0$)

$$\omega(\omega^2-\omega_c^2)\delta\psi = -\frac{1}{2}\omega\nabla^2(\psi_0 f) + \frac{1}{2}\omega\left(\frac{\nabla^2\psi_0}{\psi_0}\right)(\psi_0 f) + i\omega_c(\nabla\psi_0\times\nabla f)\cdot\hat{\mathbf{z}}. \tag{30}$$

Here, $\omega_c = eB^{\rm ext}/m^\star c$ is the cyclotron frequency expressed in natural units. Making explicit use of the periodicity of the system in both spatial directions, we can write the fluctuating part of the von Weizsäcker wave function in the form

$$\delta\psi(\mathbf{r},t) = e^{i(\mathbf{q}\cdot\mathbf{r}-\omega t)}\sum_{\mathbf{G}} c_{\mathbf{G}} e^{i\mathbf{G}\cdot\mathbf{r}}, \tag{31}$$

where $c_{\mathbf{G}}$ is a Fourier expansion coefficient, $\mathbf{q}$ is a 2D Bloch wave vector restricted to the first Brillouin zone, and $\mathbf{G} = (2\pi m/a_x, 2\pi n/a_y)$, with $m,n = 0,\pm1,\pm2,\ldots$, are reciprocal lattice vectors. The plane-wave basis functions satisfy the orthonormality condition

$$\frac{1}{\mathcal{A}}\int_{\mathcal{A}} d^2\mathbf{r}\, e^{-i(\mathbf{G}-\mathbf{G}')\cdot\mathbf{r}} = \delta_{\mathbf{G}\mathbf{G}'}, \tag{32}$$

where $\mathcal{A} = a_x a_y$ is the area of a unit cell. Expanding the product $(\psi_0 f)$ in a similar way, viz.,

$$(\psi_0 f) = \psi_0\delta v_{\rm eff} + \frac{\lambda_w}{2}\frac{\nabla^2\psi_0}{\psi_0}\delta\psi - \frac{\lambda_w}{2}\nabla^2\delta\psi = e^{i(\mathbf{q}\cdot\mathbf{r}-\omega t)}\sum_{\mathbf{G}} f_{\mathbf{G}} e^{i\mathbf{G}\cdot\mathbf{r}}, \tag{33}$$

and substituting these expansions into Eq. (30), we obtain the nonlinear eigenvalue equation

$$\omega(\omega^2-\omega_c^2)c_{\mathbf{G}} = \omega\sum_{\mathbf{G}'} B_{\mathbf{G}\mathbf{G}'} f_{\mathbf{G}'} + \omega_c\sum_{\mathbf{G}'} A_{\mathbf{G}\mathbf{G}'} f_{\mathbf{G}'}, \tag{34}$$

where

$$B_{\mathbf{G}\mathbf{G}'} \equiv \frac{1}{2}(\mathbf{q}+\mathbf{G})^2\delta_{\mathbf{G}\mathbf{G}'} + \frac{1}{\lambda_w}(v_{\rm eff}-\mu)[\mathbf{G}-\mathbf{G}'], \tag{35}$$

and

$$A_{\mathbf{G}\mathbf{G}'} \equiv i[\mathbf{q}\times(\mathbf{G}-\mathbf{G}') + (\mathbf{G}\times\mathbf{G}')]\cdot\hat{\mathbf{z}}\ln\psi_0[\mathbf{G}-\mathbf{G}']. \tag{36}$$

We adopt the notation that square braces denote a Fourier-transformed variable.

The Fourier coefficients $f_{\mathbf{G}}$ are connected to the fluctuating wave-function expansion coefficients $c_{\mathbf{G}}$ through Eq. (33), viz.,

$$f_{\mathbf{G}} = \sum_{\mathbf{G}'}\left[M^K_{\mathbf{G}\mathbf{G}'} + M^X_{\mathbf{G}\mathbf{G}'} + M^H_{\mathbf{G}\mathbf{G}'} + \lambda_w B_{\mathbf{G}\mathbf{G}'}\right]c_{\mathbf{G}'} \equiv \sum_{\mathbf{G}'}\tilde{M}_{\mathbf{G}\mathbf{G}'}c_{\mathbf{G}'}, \tag{37}$$

and

$$M^K_{\mathbf{G}\mathbf{G}'} = 2\pi\psi_0^2[\mathbf{G}-\mathbf{G}']$$

$$M^X_{\mathbf{G}\mathbf{G}'} = -\sqrt{\frac{8}{\pi}}\psi_0[\mathbf{G}-\mathbf{G}'] \tag{38}$$

$$M^H_{\mathbf{G}\mathbf{G}'} = 4\pi\sum_{\mathbf{G}''}\frac{\psi_0[\mathbf{G}-\mathbf{G}'']\psi_0[\mathbf{G}''-\mathbf{G}']}{\sqrt{(q_x+G_x'')^2+(q_y+G_y'')^2}},$$

are the kinetic, exchange, and Hartree matrices that arise when the $\psi_0\delta v_{\rm eff}$ term is Fourier transformed. The eigenvalues $\omega$ of Eq. (34) give the excitation frequencies of the system, and the corresponding eigenvectors $\vec{c}$ can be used to determine the density fluctuation of the collective mode.

Equation (34) represents an infinite dimensional matrix problem that, for practical purposes, must be solved on some subset of the 2D reciprocal lattice vectors. Any truncation of the basis set must be checked to ensure that the results for the modes of interest do not depend on the number of $\mathbf{G}$ vectors retained. If the system is weakly modulated, the coupling between different reciprocal lattice vectors is likewise weak, and the matrix problem is only of a modest size. However, if the system is strongly modulated with a large unit cell ($a \gtrsim 800$ nm), the number of basis functions required to adequately describe the dynamics of the system can become unmanageably large. This is a possible limitation of the plane-wave expansion technique.

Since our main interest is in making contact with the experimental FIR data, we shall only consider the $\mathbf{q}=0$ limit of our calculations.[26] In this situation, our dynamical equations are invariant with respect to the point group $C_{4v}$ (for $a_x = a_y$) when $\omega_c = 0$. A nonzero magnetic field lowers the symmetry of the system to $C_4$ because of the additional term involving the $A_{\mathbf{G}\mathbf{G}'}$ matrix in Eq. (34). In either case, we can appeal to the inherent symmetry of the reciprocal space to substantially reduce the number of effective basis vectors considered in a calculation. The way in which this is done is discussed in Appendix A.

### C. Power absorption

We now consider the response of the system to a spatially uniform radiation field incident normally on the sample and polarized in the $x$ direction: $\mathbf{E}^{\rm ext}(\mathbf{r},t)=\frac{1}{2}E_0(e^{-i\omega t}+e^{i\omega t})\hat{\mathbf{x}}$. This is the most direct way of making contact with experiments, which probe the collective excitations of the system by means of FIR spectroscopy.

The physically relevant quantity is the time averaged power absorption, which is given by[23]

$$\langle P\rangle_t=\left\langle \int d^2\mathbf{r}\,\mathbf{j}^{\rm ind}(\mathbf{r},t)\cdot\mathbf{E}^{\rm ext}(\mathbf{r},t)\right\rangle_t$$
$$=\frac{1}{2}E_0\ \ {\rm Re}\int d^2\mathbf{r}\,j_x^{\rm ind}(\mathbf{r},\omega), \tag{39}$$

where $j_x^{\rm ind}(\mathbf{r},\omega)=-n_0(\mathbf{r})v_x(\mathbf{r},\omega)$ is the induced current density and the velocity is now a solution of

$$\frac{\partial\mathbf{v}}{\partial t}=-\gamma\mathbf{v}+\delta\mathbf{F}^{\rm tot}-\mathbf{v}\times\mathbf{B}^{\rm ext}. \tag{40}$$

The total fluctuating force includes the external contribution $\delta\mathbf{F}^{\rm ext}=-\mathbf{E}^{\rm ext}$. In addition, we have introduced a phenomenological relaxation rate $\gamma$, which has the effect of giving the excitations a finite lifetime. This implies that any frequency factors arising from the time-derivative of the velocity must be replaced by $\omega\rightarrow\tilde{\omega}=\omega+i\gamma$. In previous studies[12] it was found that the experimental transmission data was most faithfully reproduced by a frequency dependent relaxation rate, $\gamma=\gamma_0/\omega$. We retain the same frequency dependence here.

Noting that the current density is itself a periodic function of both spatial directions, we can write Eq. (39) as

$$\frac{\langle P\rangle_t}{A}=\frac{1}{2}E_0\ \ {\rm Re}\ \ j_x^{\rm ind}[\mathbf{G}=0,\omega], \tag{41}$$

where $A$ is the sample area and

$$j_x^{\rm ind}[\mathbf{G},\omega]=\frac{1}{\mathcal{A}}\int d^2\mathbf{r}\,e^{-i\mathbf{G}\cdot\mathbf{r}}j_x^{\rm ind}(\mathbf{r},\omega) \tag{42}$$

is the Fourier coefficient of the induced current. The $\mathbf{G}=0$ component is just the average induced current within a unit cell. A straightforward calculation paralleling Ref. 23 leads to the following expression for this component

$$j_x^{\rm ind}[\mathbf{G}=0,\omega]=\frac{-2\tilde{\omega}}{\tilde{\omega}^2-\omega_c^2}\sum_{\mathbf{G}'}G_x'\psi_0[\mathbf{G}']f_{\mathbf{G}'}$$
$$+\frac{2i\omega_c}{\tilde{\omega}^2-\omega_c^2}\sum_{\mathbf{G}'}G_y'\psi_0[\mathbf{G}']f_{\mathbf{G}'}+\frac{i\tilde{\omega}n_0[\mathbf{G}=0]E_0}{\tilde{\omega}^2-\omega_c^2}. \tag{43}$$

The net effect of including an external driving field $\mathbf{E}^{\rm ext}$ was previously shown to convert the nonlinear eigenvalue problem in Eq. (34), into a set of inhomogeneous equations[23]

$$\omega(\tilde{\omega}^2-\omega_c^2)c_{\mathbf{G}}-\tilde{\omega}\sum_{\mathbf{G}'}B_{\mathbf{G}\mathbf{G}'}f_{\mathbf{G}'}-\omega_c\sum_{\mathbf{G}'}A_{\mathbf{G}\mathbf{G}'}f_{\mathbf{G}'}=b_{\mathbf{G}}, \tag{44}$$

where

$$b_{\mathbf{G}}=-E_0(i\tilde{\omega}G_x-\omega_cG_y)\psi_0[\mathbf{G}]. \tag{45}$$

The $\mathbf{q}=0$ solution of Eq. (44) along with Eq. (37) provides a complete determination of $j_x^{\rm ind}[\mathbf{G}=0,\omega]$. The substitution of Eq. (43) into Eq. (41) yields the final expression for the FIR power absorption.

## III. QUANTUM DOTS

In Sec. II, the formalism for studying a 2D modulated electronic system was developed for an arbitrary periodic confining potential $v_{\rm ext}(\mathbf{r})$. In this section, we restrict our attention to potentials that confine the electrons in all three spatial dimensions, thereby forming an array of quasi-0D quantum dots. In particular, we have in mind the experiment performed by Demel *et al.*[4,5] in which an array of quantum dots was prepared from modulation–doped $Al_xGa_{1-x}As/GaAs$ heterostructures. In this experiment, resonant anticrossings were observed in the magnetic dispersions for arrays of dots with $N=25$ and $N=210$ electrons per dot. These anticrossings were tentatively explained in terms of a nonlocal interaction associated with the finite compressibility of the electron gas,[4,5] although subsequent work pointed to the importance of noncircular perturbations. Here, we explore the origin of these anticrossings in greater detail by systematically studying confining potentials of the form

$$v_{\rm ext}(r,\theta)=\frac{1}{2}kr^2+\frac{1}{4}pr^4+\frac{1}{4}p\varepsilon r^4\cos(4\theta), \tag{46}$$

where $\theta$ is the azimuthal angle in polar coordinates. For $p=0$, we have parabolic confinement with $\omega_0=\sqrt{k}$. Setting $\varepsilon=0$ with $k,p\neq0$ introduces a quartic radial perturbation, and finally, if all three parameters are nonzero, the last term in Eq. (46) breaks the circular symmetry of the potential. It is understood that the potential in Eq. (46) is centered in the unit cell and periodically extended throughout the array. Since the dots of interest are localized near the center of the cell, the behavior of the potential near the cell boundaries is of no consequence.

In order to make contact with previous work on this problem, it will prove useful to elaborate on the various parameters appearing in Eq. (46). To begin, we set $\varepsilon=0$. Following Ref. 12, we define the anharmonicity parameter $\eta\equiv pR_0^2/2k$, where $R_0$ is the radius of the dot as determined within a classical calculation that includes only the Hartree interaction of the electrons. This radius is given implicitly by the equation[12]

$$R_0=\frac{R_0^{\rm p}}{\left(1+\frac{8}{5}\eta\right)^{1/3}}, \tag{47}$$

where $R_0^{\rm p}$ is the equilibrium radius for pure parabolic confinement (hence the superscript ''p'') given by[6]

$$R_0^{\mathrm{p}}=\left[\frac{3\pi}{4}\frac{e^2N}{\epsilon k}\right]^{1/3}. \tag{48}$$

It was further shown in Ref. 12 that the zero-field ($B=0$) frequency of the lowest dipolar mode is given to an excellent approximation by

$$\omega_0'=\omega_0\sqrt{1+\frac{8}{5}\eta}, \tag{49}$$

where $\omega_0$ is the bare harmonic frequency defined above. Thus, in the absence of a noncircular perturbation, a given zero-field dipole frequency is determined by a family of $\omega_0$ and $\eta$ values. These values are adjusted to reproduce the experimentally observed frequency $\omega_0'$, as well as other features of the observed absorption spectrum. In this way, the quantities $k$ and $p$ can be determined. We observe from our calculations that the subsequent inclusion of the parameter $\varepsilon$ has a negligible effect on $\omega_0'(B=0)$, so that the effect of this parameter can be investigated independently of the other two. Typical values for $\eta$ and $\varepsilon$ used in the calculations lie in the range $[0,1]$.

Finally, we summarize the appropriate physical parameters for the $Al_xGa_{1-x}As/GaAs$ heterostructures under consideration: the effective Bohr radius $a_0^\star$ is 103 Å and the effective Rydberg of energy, $\mathrm{Ry}^\star=e^2/2\epsilon a_0^\star$, is 5.4 meV. To be as consistent as possible with the experimental situation,[4] we focus on dot arrays with $N=210$ electrons per dot and a FIR zero field absorption frequency of $\omega_0'=32\ \mathrm{cm}^{-1}$.

### A. Parabolic confinement

As mentioned above, $\eta=0$ provides a potential that defines an array of parabolically confined dots. The nature of the collective excitations for such a system are by now well established in the literature.[6–12,27–34] In Fig. 1(a) we show the calculated ground-state density for a square array with $a_x=a_y=1000$ nm containing well-separated dots with $N=210$ electrons per dot. The radius of the dot is about 150 nm, and for the sake of clarity, we show only that portion of the unit cell in which the electronic density is localized. The radius found here on the basis of the TFDW functional is similar to the value obtained using Eq. (48), viz., $R_0^{\mathrm{p}}=160$ nm, with $\omega_0=32\ \mathrm{cm}^{-1}$ and $N=210$. The similarity of these values indicates that the Hartree interaction is in fact dominating the equilibrium distribution and that the exchange and kinetic energies are playing a relatively minor role. The shape of the distribution is approximately semicircular as found in the classical calculation,[12] but with a smooth variation at the edge of the dot as a result of the von Weiszäcker correction. This term in the energy functional allows us to simulate the behavior of the charge density expected within a fully quantum-mechanical calculation.

It is perhaps worth emphasizing that the equilibrium calculations described above effectively correspond to *isolated* quantum dots. The Coulomb interactions between equilibrium charge densities in different cells of the array are eliminated, so that only intracell Coulomb interactions are retained in the calculation. Of course the potential within a given cell arises from all other charges in the system, and one should view the parabolic confining potential as the net effect of all these other charges. However, when calculating the magnetoplasmons, the intercell Coulomb interactions arising from the density fluctuations are *not* neglected. These multipolar interactions are required in order to simulate the response of an array of coupled dots. We shall examine shortly the importance of these interdot Coulomb interactions.

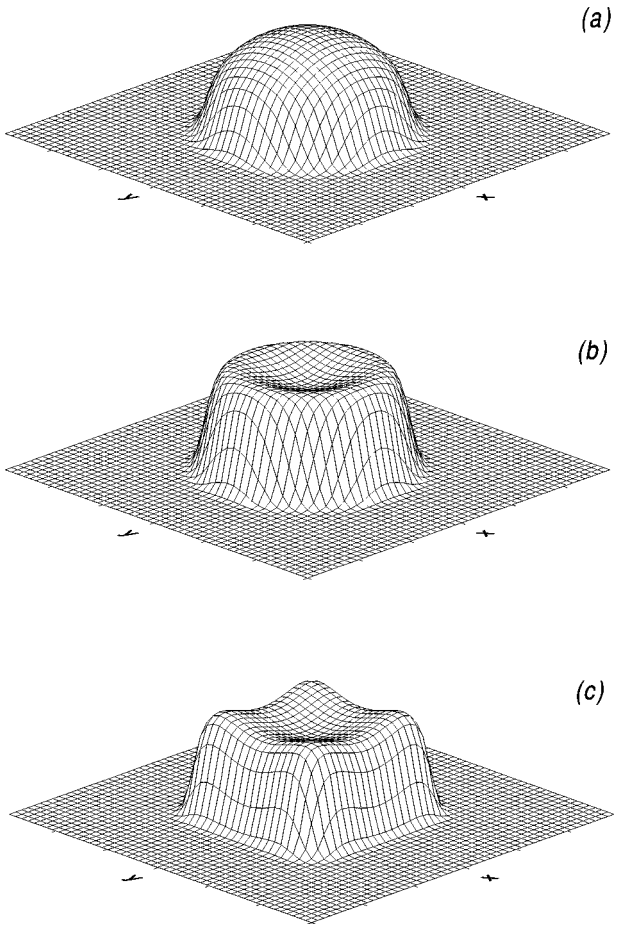


FIG. 1. Equilibrium density distributions for various confinement geometries: (a) parabolic confinement, (b) radial anharmonicity, and (c) noncircular symmetry. Parameters defining the confinement potential are given in the text. In all cases the dots are arranged on a square lattice with $a_x=a_y=1000$ nm, and contain $N=210$ electrons.

In Fig. 2, we show the calculated magnetic dispersion for the array of dots described above. To avoid cluttering the diagram, we have chosen to omit the large number of edge modes, which start from $\omega=0$ at $B=0$ and lie below $\omega=\omega_c$. These modes make no observable contribution to the power absorption and are therefore of little interest in the present paper. The mode frequencies found here are very similar to those found in the classical approximation[6] and can be classified according to the local $SO(2)$ symmetry of circularly symmetric confining potentials. As discussed in Appendix A, the Lie group $SO(2)$ has $m$ one-dimensional irreducible representations given by $\chi^m(\phi)=e^{im\phi}$, with $0\leqslant\phi\leqslant 2\pi$, and $m\in Z$. The different branches seen crossing in Fig. 2 correspond to different irreducible representations of $SO(2)$ (see Table I), and thus one would not expect any mode repulsion in the absence of some perturbation. Since the only possible perturbation in the present situation is the

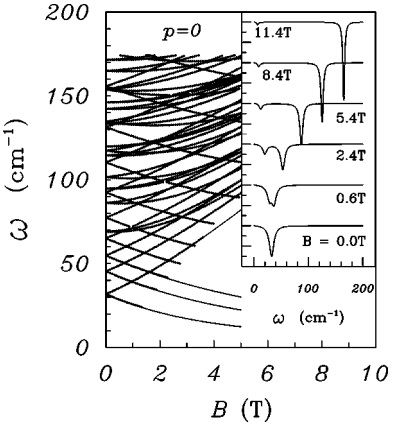


FIG. 2. The magnetic dispersion for an array of well separated parabolically confined dots. The solid circles are the numerical solutions to Eq. (34) and the solid curves are fits to Eq. (50). The figure inset shows the calculated FIR power absorption for a range of magnetic fields. The parameters defining the dots are the same as used to generate Fig. 1(a).

dynamic intercell Coulomb interaction, the results shown here confirm that this interaction is very weak. As we shall see, the effect of interdot interactions can be made apparent by reducing the interdot separation.

Within the classical theory, a subset of the dot modes has a dispersion given by the expression[6,8,12]

$$\omega_{j,\pm}=\sqrt{\Omega_j^2+(\omega_c/2)^2}\pm\omega_c/2. \tag{50}$$

The solid curves in Fig. 2 show some fits to Eq. (50), and demonstrate that the field dependence is well reproduced even though the TFDW values of $\Omega_j$ are slightly different from the analytic classical values. The lowest pair of curves corresponds to the two circular polarizations of the center-of-mass (CM) mode. According to the generalized Kohn theorem,[35] the exact separability of the $N$-body Hamiltonian into CM and relative coordinates for parabolic confinement ensures that $\Omega_1=\omega_0$ ($\omega_0=32$ cm$^{-1}$ in this case), and that only these dipole modes couple to a uniform external electric field. This fact is illustrated in the inset to Fig. 2 where we show the calculated FIR power absorption for the dot array for a range of magnetic fields consistent with the experiment in Ref. 4. The single peak at $\omega(B=0)=32$ cm$^{-1}$ reflects the fact that our model satisfies the generalized Kohn theorem. It is also clear from this figure that the two-peak structure appearing for $B\neq 0$, corresponds to the CM-mode dispersion seen in Fig. 2.

TABLE I. Compound characters for some of the $SO(2)$ representations of the point group $C_4$.

| $m^\pi$ | $E$ | $C_4$ | $C_4^2$ | $C_4^3$ |
|---|---|---|---|---|
| $0^+$ | 1 | 1 | 1 | 1 |
| $0^-$ | 1 | 1 | 1 | 1 |
| $1^+$ | 1 | $i$ | $-1$ | $-i$ |
| $1^-$ | 1 | $-i$ | $-1$ | $i$ |
| $2^+$ | 1 | $-1$ | 1 | $-1$ |
| $2^-$ | 1 | $-1$ | 1 | $-1$ |
| $3^+$ | 1 | $-i$ | $-1$ | $i$ |
| $3^-$ | 1 | $i$ | $-1$ | $-i$ |

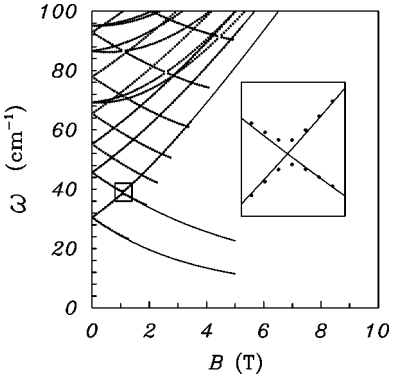


FIG. 3. The magnetic dispersion for an array of closely spaced dots. The only difference between this figure and Fig. 2 is a reduction of the lattice periodicity: $a_x=a_y=600$ nm. The consequences of this shorter periodicity are a softening of the $\omega_0$ frequency and the appearance of small anticrossings. Inset: An expanded view of the boxed region $\approx$(1.4 T,39 cm$^{-1}$) clearly showing the mode anticrossings.

We next consider the effects of interdot Coulomb coupling on the magnetoplasmon excitations. We have already indicated that this interaction is weak for a lattice constant of $a=1000$ nm, and we now support this assertion by observing the effect of reducing the lattice constant to $a=600$ nm. Figure 3 shows a small section of the magnetic dispersion for this case. Although this dispersion looks similar to Fig. 2, there are some important differences.

First, we notice a slight redshift of the $\omega_0(B=0)$ frequency while the higher-lying modes have moved slightly in the opposite direction. The softening of the $\omega_0(B=0)$ frequency can be explained by invoking the interaction between the induced dipoles on each lattice site. For the square lattice being considered, the electric field experienced by the $m$th dipole due to all other dipoles is given by[36]

$$E_m=\frac{1}{a^3}\sum_{l,n}{}'\frac{1}{(l^2+n^2)^{3/2}}\left[\frac{3l^2}{l^2+n^2}-1\right]p_{m+l}, \tag{51}$$

where we have assumed, consistent with Sec. II C, that the polarization is in the $\hat{\mathbf{x}}$ direction. The quantities $l$ and $n$ identify positions on the 2D lattice, viz., $\mathbf{r}=la\hat{\mathbf{x}}+na\hat{\mathbf{y}}$, and the primed summation indicates that the $n=l=0$ point is excluded. In the FIR regime, each of the dipole moments $p_m$ has a common magnitude $p_0$, and the electric field can be written as

$$E_m=\frac{p_0}{a^3}S, \tag{52}$$

where

$$S=\sum_{l,n}{}'\frac{1}{(l^2+n^2)^{3/2}}\left[\frac{3l^2}{l^2+n^2}-1\right]. \tag{53}$$

The quantities $p_m$ and $E_m$ are connected through the relation $p_m=\alpha(\omega)E_m$ where $\alpha(\omega)$ is the dipole polarizability of the

TABLE II. Character table for the irreducible representations of the point group $C_4$.

| $C_4$ | $E$ | $C_4$ | $C_4^2$ | $C_4^3$ |
|---|---|---|---|---|
| $D_1$ | 1 | 1 | 1 | 1 |
| $D_2$ | 1 | $-1$ | 1 | $-1$ |
| $D_3$ | 1 | $i$ | $-1$ | $-i$ |
| $D_4$ | 1 | $-i$ | $-1$ | $i$ |

dot. For parabolic confinement, the polarizability is given by $\alpha(\omega)=Ne^2/m^\star(\omega_0^2-\omega^2)$. Using this result in Eq. (52), we find the following frequency for the CM mode

$$\omega^2=\omega_0^2-\frac{S}{4\pi}\omega_p^2, \tag{54}$$

where $\omega_p^2=4\pi Ne^2/\epsilon m^\star a^3$ is the effective plasmon frequency. This simple result shows that the interdot dipole interactions decrease the absorption frequency from that of a single dot.

Next, we note the appearance of small anticrossings in the magnetic dispersion that was not discernible for the well-separated dots. These anticrossings are still difficult to resolve, so in the figure inset, we show a close-up view of the boxed region, which clearly illustrates the mode repulsion. These anticrossings arise because the interdot coupling of the dots on the square lattice breaks the *local* circular symmetry of the confining potential. Specifically, the square symmetry of the lattice is lower than the local SO(2) symmetry of the dots. As shown in Appendix A, the $1^+$ and $3^-$ modes now transform under the same irreducible representation of $C_4$ (see Table II), which means that the modes will repel (anticross) each other under a reduction of the symmetry. We stress however that these anticrossings are far too weak to account for the mode anticrossings observed in the Demel *et al.* experiments.

### B. Radial anharmonic confinement

The inclusion of a perturbative term of the form $\delta v_{\rm ext}(r)=\frac{1}{4}pr^4$ in Eq. (46) preserves the circular symmetry of the confining potential, but allows for the mixing of different dipole modes with a redistribution of the FIR oscillator strength. The ground state density is illustrated in Fig. 1(b) and is qualitatively similar to that found in the classical model.[12] This density was generated with $\omega_0=20\ \ {\rm cm}^{-1}$ and $\eta=1$. The circular ridge is a result of the $r^4$ perturbation. The calculated magnetic dispersion and FIR power absorption are shown in Fig. 4.

Comparing Figs. 2 and 4, we see that many of the features of the magnetic dispersion in the case of parabolic confinement are still present for the anharmonic potential. To emphasize this point, we have plotted the dispersions described by Eq. (50) using $\Omega_j$ as an adjustable parameter. We see that Eq. (50) provides a good fit to the data, and indicates that the functional form of the magnetic dispersion is not sensitive to the form of the confining potential. In particular, a fit of this dispersion to the lowest CM modes does *not* in general provide a direct measurement of the harmonic term in the confining potential. The relative spacing between the CM modes

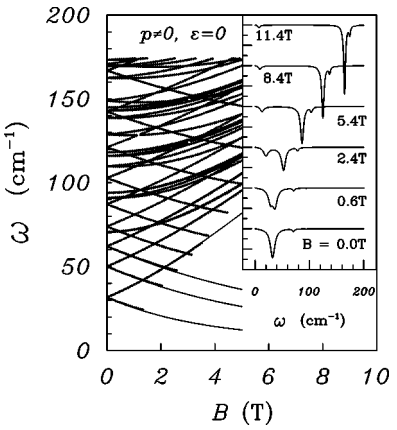


FIG. 4. The magnetic dispersion for an array of radially anharmonic dots. The solid circles are the numerical solutions to Eq. (34) and the solid curves are fits to Eq. (50). The parameters are the same as those used to generate Fig. 1(b). The inset shows the calculated FIR power absorption.

and the higher modes does depend on the anharmonicity, but the latter are not usually observable in FIR experiments.

The main observable difference between parabolic and radially anharmonic confinement is revealed by the theoretical power absorption in the inset to Fig. 4. The curves were generated for a range of magnetic fields corresponding to the experimental situation in Ref. 4. The dominant dipolar peaks found for parabolic confinement are now accompanied by a weak satellite which tracks along the $\omega_+$ CM-like mode. The oscillator strength of the satellite is directly controlled by the parameter $\eta$. A value of approximately 1 reproduces the observed oscillator strength at high fields, while the harmonic confining frequency was adjusted to $\omega_0=20\ \ {\rm cm}^{-1}$ in order to yield a $B=0$ dipole frequency of 32 $\rm cm^{-1}$. These parameters imply a strong anharmonicity. The $B=0$ peak at $\omega=32\ \ {\rm cm}^{-1}$ in Fig. 4 can therefore no longer be identified as a CM mode in the sense of parabolic confinement. The very appearance of the satellite is an indication that the generalized Kohn theorem is no longer valid. The $r^4$ perturbation has the effect of coupling the dipolar modes found in the parabolic limit,[12] thereby making other dipole modes FIR active. A comparison of our calculated FIR power absorption to the experimental data[4] leaves little doubt that the satellite structure observed in the experiment has its origins in the anharmonicity of the confining potential. This conclusion confirms that reached by other workers using different theoretical approaches.[9,10,12] The power absorption thus provides a direct probe for determining the geometry of the confining potential.

Finally, we mention that calculations were also carried out for the reduced lattice spacing of 600 nm. As in the case of parabolic confinement, anticrossings in the magnetic dispersion arise, but the strength of these anticrossings is again too weak to account for those observed experimentally. We can therefore rule out interdot Coulomb interactions as a significant mechanism at the experimental interdot separations.

### C. Noncircular confinement

We now consider an explicit symmetry breaking perturbation of the form given in Eq. (46) with $\varepsilon\neq 0$. It is clear

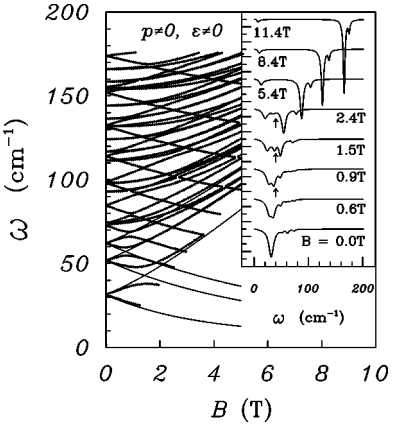


FIG. 5. The magnetic dispersion for an array of noncircular dots. The solid circles are the numerical solutions to Eq. (34) and the solid curves are fits to Eq. (50). The same parameters as in Fig. 1(c) are used to generate this figure. The inset shows the calculated FIR power absorption. The size and position of the pronounced anticrossing at $\omega \approx 40$ cm$^1$ ($\uparrow$) are in quantitative agreement with experiment. For $B > 3$ T, the power absorption is almost indistinguishable from Fig. 4.

that such a perturbation is consistent with the geometry of the dots studied in Ref. 4. The equilibrium density for the noncircular confining potential is shown in Fig. 1(c). This density profile was generated with $N=210$, $\omega_0 = 20$ cm$^{-1}$, $\eta = 1$, $\varepsilon = 0.4$, and $a_x = a_y = 1000$ nm. The maximal radial extent of this dot is about 155 nm. It is clear from Fig. 1(c) that the deviation from circular symmetry is very pronounced, and one should not expect the same mode dispersions as obtained for arrays of circularly symmetric dots.

Turning to the magnetic dispersion in Fig. 5, we do indeed find a very different $B$-field dependence of the collective modes. Specifically, we note the appearance of strong anticrossings between the lowest-lying modes, and progressively weaker anticrossings for the higher modes. These anticrossing are a consequence of the $\delta v_{\rm ext}(r,\theta) = \frac{1}{4} p \varepsilon r^4 \cos(4\theta)$ perturbation in Eq. (46), and occur when the angular momentum of the symmetric modes differ by an integral multiple of four. The lowest anticrossing is between a pair of $m=1$ and $m=-3$ modes and is the most important since it is the structure observed in the Demel *et al.* experiment. A comparison of Fig. 5 with Fig. 2 of Ref. 4 shows that our results are in good agreement with regard to the size and location of the anticrossing. Once again, the solid curves in Fig. 5 are fits to Eq. (50) and here, they serve to emphasize the difference between circular and noncircular confinement geometries.

The magnitude of the gap occurring at each anticrossing is directly related to the parameter $\varepsilon$. The value $\varepsilon = 0.4$ was chosen to best fit the observed transmission data[4] and the inset to Fig. 5 shows our calculated power absorption. At low fields there is weak structure to the high-field side of the main resonance, which is probably too weak to be resolved experimentally. However, as one enters the field range of the anticrossing between 1 and 2 T, a new peak appears and leads to an absorption spectrum consisting of three peaks. This structure is most distinct at a field of $B = 1.5$ T which is in the middle of the anticrossing region. By $B = 2.4$ T, the central peak has already lost most of its oscillator strength, and the power absorption takes on the characteristics of the $r^4$ power spectrum of Fig. 4, including the high-field satellite. This overall behavior is entirely consistent with experiment.[4]

## IV. CONCLUSIONS

In this paper, we have presented a generalization of our previous work[23] on TFDW hydrodynamics in laterally modulated electronic systems. As a specific application, we have examined the magnetoplasmon excitations in arrays of both circular and noncircular dots. By considering potentials, which include both radial and noncircular anharmonic perturbations, we are able to fully explore the effects of geometric confinement on the magnetoplasmon excitations of the dots.

In the case of circular dots, our results indicate that an $r^4$ radial perturbation can account for the satellite-peak structure observed in the experiments.[4,5,12] We have also seen that the interdot coupling is too weak at the experimental lattice constant to give rise to any discernible anticrossing effects, in agreement with earlier results.[27] These effects only become apparent when the lattice spacing is reduced to the order of the size of a dot.

On the other hand, the addition of a noncircular perturbation of the form $r^4\cos(4\theta)$ was shown to induce anticrossings in the magnetoplasmon dispersion that are entirely consistent with the experimentally observed transmission data. Specifically, the location for the onset of the first optically observable anticrossing, along with higher $B$-field peak structure, was found to be in good agreement with experiment. Based on this result, we conclude that only an explicit noncircular symmetry in the confining potential can fully account for the mode anticrossings observed in the experiments.[4,5]

The work presented here is applicable to a wide variety of 2D geometrical confinements. Our current interest lies in the application of this formalism to antidot arrays, which are complementary structures to quantum dot arrays. Recent experimental work on these systems has revealed a collective excitation spectrum very different from the dot arrays.[37,38] A detailed discussion of these systems will be presented elsewhere.

## ACKNOWLEDGMENTS

This work was supported by a grant from the Natural Sciences and Engineering Research Council of Canada.

## APPENDIX: DERIVATION OF THE SYMMETRY-REDUCED DYNAMICAL EQUATIONS

The square primitive cell of our problem results in a reciprocal lattice with fourfold symmetry, as illustrated in Fig. 6. The point group of the square lattice is $C_{4v}$, and the full point symmetry is $C_{4v} \otimes (E,T)$, where $(E,T)$ is the time-reversal symmetry group and $E$ is the identity element.[39] In the context of our problem, we recall that we are primarily interested in the calculation of the FIR response of the system, which corresponds to the $\mathbf{q}=0$ limit of the general set of inhomogeneous equations, Eq. (44). In the absence of a magnetic field, these equations are invariant under $C_{4v}$

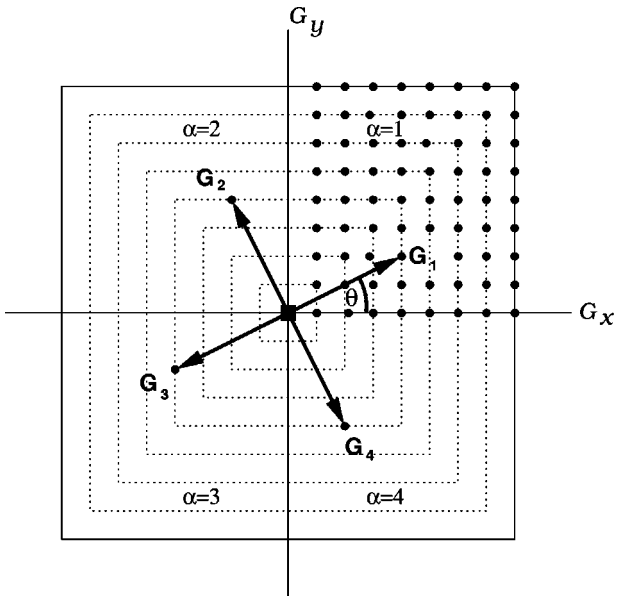


FIG. 6. A schematic representation of the truncated 2D reciprocal lattice with point group symmetry $C_{4v}$. The arrows are an example of a shell of vectors $\{|\mathbf{G}_\alpha\rangle\}$ which are generated from $\mathbf{G}_1$ by the symmetry operation $C_4$. The solid circles illustrate the set of $\mathbf{G}$ vectors used in the symmetry-reduced calculation; a square array of points is retained to facilitate the use of fast Fourier transforms.

$\otimes(E,T)$, however the inclusion of a magnetic field breaks time-reversal symmetry and lowers the symmetry of the system from $C_{4v}\rightarrow C_4$. This is easily seen if one observes the symmetry group of the $A_{\mathbf{GG}'}$ matrix in Eq. (36). It follows that $C_4$ is the relevant group symmetry to consider in the most general case (i.e., magnetoplasma excitations).

Let us step back for a moment, and consider the full symmetry group of the square lattice, namely, $C_{4v}=\{E,C_4,C_4^3,C_4^2,m_x,m_y,\sigma_u,\sigma_v\}$, where $m$ are reflections about the $x$ or $y$ axes, and $\sigma$ is a reflection about a diagonal of the square. We can construct a representation, $\Gamma$ [we use this notation to remind us that we are at the $\Gamma$ point of the first Brillouin zone (BZ)], of this group by considering a function space spanned by the set of functions $\{|\mathbf{G}_i\rangle\}$. One natural choice would be to consider the set of functions defined by $|\mathbf{G}_i\rangle\equiv a^{-1}e^{i\mathbf{G}_i\cdot\mathbf{r}}$ with $1\leqslant i\leqslant 4$ as shown in Fig. 6. If we choose as our canonical function $|\mathbf{G}_1\rangle$, the other functions are obtained by acting with the $C_4$ operator on the function $|\mathbf{G}_1\rangle$: $C_4^n\ |\mathbf{G}_1\rangle = |\mathbf{G}_{1+n}\rangle$, with $|\mathbf{G}_5\rangle\equiv|\mathbf{G}_1\rangle$. Since the generators of the group $C_{4v}$ are $\{C_4,m_x\}$, we need only obtain the representations for the generators of $C_{4v}$ to construct the entire representation of the group. It is easy to show that generators of $C_{4v}$ in this representation take the form

$$\Gamma(C_4)=\begin{bmatrix}0&1&0&0\\0&0&1&0\\0&0&0&1\\1&0&0&0\end{bmatrix}\quad\Gamma(m_x)=\begin{bmatrix}0&0&0&1\\0&0&1&0\\0&1&0&0\\1&0&0&0\end{bmatrix},\tag{A1}$$

and that the characters for $C_{4v}$ are given by

TABLE III. Character table for the irreducible representations of the point group $C_{4v}$.

| $C_{4v}$ | $E$ | $2C_4$ | $C_4^2$ | $2m$ | $2\sigma$ |
|---|---|---|---|---|---|
| $\Gamma_1$ | 1 | 1 | 1 | 1 | 1 |
| $\Gamma_2$ | 1 | −1 | 1 | 1 | −1 |
| $\Gamma_3$ | 1 | 1 | 1 | −1 | −1 |
| $\Gamma_4$ | 1 | −1 | 1 | −1 | 1 |
| $\Gamma_5$ | 2 | 0 | −1 | 0 | 0 |

| $C_{4v}$ | $E$ | $2C_4$ | $C_4^2$ | $2m$ | $2\sigma$ |
|---|---|---|---|---|---|
| $\Gamma$ | 4 | 0 | 0 | 0 | 2. |

The character table for the irreducible representation of $C_{4v}$ is shown in Table III. Since there is no four-dimensional irreducible representation of $C_{4v}$, $\Gamma$ must be reducible. It is a simple matter of class-wise character addition to determine that the $\Gamma$ representation must be decomposed according to $\Gamma=\Gamma_1\oplus\Gamma_4\oplus\Gamma_5$.

Now, let us consider the dipole operator $\boldsymbol{\mu}=e\mathbf{r}$. This operator generates the representation $\Gamma_{\boldsymbol{\mu}}=\Gamma_1\oplus\Gamma_5$ under $C_{4v}$. The $\Gamma_1$ representation is derived from the $z$ component of $\mathbf{r}$, whereas the $\Gamma_5$ representation is induced by the $(x,y)$ components. Owing to the fact that we are only considering radiation polarized in the plane of the 2DEG, we can immediately see that the invariant subspace of $\Gamma_5$ contains all of the dipole active modes of our problem. Thus, rather than concerning ourselves with solving the generalized set of equations, viz., Eq. (44), we can use the symmetry of the system to solve for only those eigenvalues that will be of interest in a FIR-mode calculation.

The problem of projecting into the $\Gamma_5$ representation is really a matter of block-diagonalizing our system of equations and picking out that block associated with $\Gamma_5$. This amounts to finding a unitary transformation that will block diagonalize each of the $\Gamma$ matrices of the group $C_{4v}$. Motivated by the knowledge that under a nonzero magnetic field the group symmetry is $C_4$, we consider the eigenvalues and eigenvectors of the group element $C_4\in C_4$. Indeed, since $C_4$ is the generator of the point group $C_4$, it is the only group element that we need to consider. A simple calculation reveals that the eigenvalues and normalized eigenvectors of $\Gamma(C_4)$ are

$$\lambda^{(1)}=1\quad|v^{(1)}\rangle=\frac{1}{2}\begin{bmatrix}1\\1\\1\\1\end{bmatrix};\quad\lambda^{(2)}=-1\quad|v^{(2)}\rangle=\frac{1}{2}\begin{bmatrix}1\\-1\\1\\-1\end{bmatrix}$$

$$\lambda^{(3)}=i\quad|v^{(3)}\rangle=\frac{1}{2}\begin{bmatrix}1\\i\\-1\\-i\end{bmatrix};\quad\lambda^{(4)}=-i\quad|v^{(4)}\rangle=\frac{1}{2}\begin{bmatrix}1\\-i\\-1\\i\end{bmatrix}.\tag{A2}$$

The four normalized eigenvectors $|v^{(\lambda)}\rangle$ are applied in this order to produce the unitary matrix $U$, and its inverse $U^{-1}$

$$U=\frac{1}{2}\begin{bmatrix}1 & 1 & 1 & 1\\ 1 & -1 & i & -i\\ 1 & 1 & -1 & -1\\ 1 & -1 & -i & i\end{bmatrix}$$

$$U^{-1}=\frac{1}{2}\begin{bmatrix}1 & 1 & 1 & 1\\ 1 & -1 & 1 & -1\\ 1 & -i & -1 & i\\ 1 & i & -1 & -i\end{bmatrix}. \tag{A3}$$

For example, applying $U$ to the group element $C_4$ yields

$$U^{-1}C_4U=\begin{bmatrix}1 & 0 & 0 & 0\\ 0 & -1 & 0 & 0\\ 0 & 0 & i & 0\\ 0 & 0 & 0 & -i\end{bmatrix}. \tag{A4}$$

The unitary transformation matrix, $U$, will block diagonalize all of the $\Gamma$ matrices for the group $C_{4v}$. In other words, the eigenvectors $\{|v\rangle\}$ of $C_4$ define a symmetrized basis for $\Gamma$ of $C_{4v}$. For the general case, $\omega_c \neq 0$, the symmetry is $C_4$, and all the matrices in the $\Gamma$ representation of $C_4$ will consist of $1\times 1$ blocks (i.e., fully diagonalized). It is now clear that the eigenvalues $\lambda^{(1)}$ and $\lambda^{(2)}$ are associated with the $\Gamma_1$ and $\Gamma_4$ irreducible representations of $C_{4v}$ respectively. The eigenvalues $\lambda^{(3)}$ and $\lambda^{(4)}$ are associated with $\Gamma_5$; the vector space spanned by their eigenvectors $(|v^{(3)}\rangle, |v^{(4)}\rangle)$ is the two-dimensional irreducible representation of $\Gamma_5$.

It is of interest to know how the irreducible representations of $C_{4v}$ relate to those of $C_4$. This can be done by appealing to the character tables for both the $C_{4v}$ and $C_4$ point groups (see Tables II and III). By inspection, we can see that

$$\begin{aligned}\Gamma_1 &\rightarrow D_1\\ \Gamma_2 &\rightarrow D_2\\ \Gamma_3 &\rightarrow D_1\\ \Gamma_4 &\rightarrow D_2\\ \Gamma_5 &\rightarrow D_3 \oplus D_4.\end{aligned} \tag{A5}$$

From Eq. (A5), we see that the two-dimensional irreducible representation $\Gamma_5$ *splits* when the symmetry is lowered from $C_{4v} \rightarrow C_4$. Note also that $D_3$ and $D_4$ are complex conjugate representations. The relevance of this fact is that in the absence of a magnetic field, these two representations are degenerate (time-reversal symmetry). The application of a magnetic field will lift this degeneracy, and one should expect two modes appearing from the $\Gamma_5$ contribution; one from each of the $D$'s appearing in its decomposition. In the context of our model, the absence of a magnetic field implies that we only require *one* of either $\lambda^{(3)}$ or $\lambda^{(4)}$ to obtain all of the FIR-active modes of the system.

It is also of interest to determine what the relations are between the irreducible representations of $C_4$ and $SO(2)$. The (compact) Lie group $SO(2)$ is the symmetry group of the circular symmetric dots. If the dots are well isolated, they are unaware of the lattice, and the modes of the system can be classified according to their transformation under $SO(2)$. If the dots are closer together (close enough to become aware of neighboring dots), then the square symmetry of the lattice will break the local $SO(2)$ symmetry. In Table I, we show the character table for some of the irreducible representation of $SO(2)$ for the point group $C_4$. What is of note is the compatibility relations between the group $SO(2)$ and $C_4$, viz.,

$$\begin{aligned}0^+ &\rightarrow D_1\\ 0^- &\rightarrow D_1\\ 1^+ &\rightarrow D_3\\ 1^- &\rightarrow D_4\\ 2^+ &\rightarrow D_2\\ 2^- &\rightarrow D_2\\ 3^+ &\rightarrow D_4\\ 3^- &\rightarrow D_3.\end{aligned} \tag{A6}$$

Notice that if we are restricting our calculations to the invariant subspace of $\Gamma_5$, we will only be projecting out the modes with *odd m*; the even modes are generated by projecting into $\Gamma_1$ and $\Gamma_4$. From these compatibility relations, we see that the modes $1^+$ and $3^-$ will mix (anticross) under the symmetry lowering from $SO(2) \rightarrow C_4$ because they both transform under the same irreducible representation of $C_4$. An examination of Table I reveals that when the symmetry is strictly $SO(2)$, these modes belong to different irreducible representations, and will therefore cross. The same argument can be used if there is an explicit symmetry breaking via the confining potential. Specifically, even if the dots are well separated, a confining potential that does not transform under $SO(2)$ will lower the symmetry of the system and cause mode mixing (anticrossing) to occur.

So far, our discussion has been restricted to an abstract square lattice. How do we apply these ideas to our problem? We note that our entire reciprocal lattice is made up of sets of reciprocal lattice vectors $\{|\mathbf{G}_{i\alpha}\rangle\}$, $(\alpha=1,\ldots,4)$, which are generated by the symmetry operation $C_4$ acting on $|\mathbf{G}_{i1}\rangle$. It is therefore sufficient to only consider the reciprocal lattice vectors within the first quadrant of the total reciprocal space. The index $i=1,\ldots,n_{max}$ labels these vectors, and the set $\{|\mathbf{G}_{i\alpha}\rangle\}$ will be referred to as a *shell*. The total number of shells retained in the calculation is $n_{max}$.

The Fourier expansion of an arbitrary function $f(\mathbf{r})$ can then be written as

$$|f\rangle=\sum_{i\alpha} f_{i\alpha}|\mathbf{G}_{i\alpha}\rangle, \tag{A7}$$

where the amplitudes $f_{i\alpha}$ are the elements of a $4n_{max}\times 1$ column vector. Each set of amplitudes $f_{i\alpha}$ $(\alpha=1,\ldots,4)$ can be expressed in terms of the eigenvectors of $\Gamma(C_4)$ as

$$f_{i\alpha}=\sum_{\lambda} f_i^{(\lambda)} v_\alpha^{(\lambda)}, \tag{A8}$$

and the orthonormality of the eigenvectors implies the inverse relation

$$f_i^{(\lambda)}=\sum_{\alpha} f_{i\alpha} v_\alpha^{(\lambda)\star}. \tag{A9}$$

The star indicates complex conjugation. Now, consider some operator $\mathcal{O}$, which is *invariant* under $C_4$. The matrix representation of the equation $\mathcal{O}|f\rangle=|d\rangle$ is given by

$$\sum_{j\beta} \mathcal{O}_{i\alpha,j\beta} f_{j\beta}=d_{i\alpha}. \tag{A10}$$

Making use of Eqs. (A8) and (A9) we find

$$\sum_{j} \mathcal{O}_{ij}^{(\lambda)} f_j^{(\lambda)}=d_i^{(\lambda)}, \tag{A11}$$

where

$$d_i^{(\lambda)}=\sum_{\alpha} d_{i\alpha} v_\alpha^{(\lambda)\star} \tag{A12}$$

$$\mathcal{O}_{ij}^{(\lambda)}=\sum_{\alpha\beta} v_\alpha^{(\lambda)\star} \mathcal{O}_{i\alpha,j\beta} v_\beta^{(\lambda)}. \tag{A13}$$

In obtaining Eq. (A11) we have used the fact that the operator $\mathcal{O}$ is diagonal in the $\Gamma(C_4)$ basis. It is clear from Eq. (A11) that each of the eigenvalues, $\lambda$, defines an independent matrix problem. This is a direct consequence of the fact that we are working in the symmetrized basis of the representation $\Gamma$ of $C_4$. Furthermore, suppose $\mathcal{O}=\mathcal{P}\mathcal{Q}$ with $\mathcal{P}$ and $\mathcal{Q}$ both invariant under $C_4$. It is easy to show that

$$\mathcal{O}_{ij}^{(\lambda)}=\sum_{k} \mathcal{P}_{ik}^{(\lambda)} \mathcal{Q}_{kj}^{(\lambda)}, \tag{A14}$$

which means that for a given $\lambda$, we need deal only with the shell matrices rather than the matrices defined over all four quadrants of the reciprocal space.

Let us now apply what we have learned to Eq. (44) in the $\mathbf{q}=0$ limit. It is readily verified that $A_{\mathbf{GG}'}$, $B_{\mathbf{GG}'}$, and $\tilde{M}_{\mathbf{GG}'}$ are invariant under the symmetry group $C_4$. Therefore, Eq. (44) can be immediately cast in terms of the symmetrized functions, viz.,

$$\omega(\tilde{\omega}^2-\omega_c^2)c_i^{(\lambda)}-\tilde{\omega}\sum_k B_{ij}^{(\lambda)}\tilde{M}_{jk}^{(\lambda)}c_k^{(\lambda)}-\omega_c\sum_k A_{ij}^{(\lambda)}\tilde{M}_{jk}^{(\lambda)}c_k^{(\lambda)} = b_i^{(\lambda)}, \tag{A15}$$

where we recall that summations are over the shell index. In obtaining Eq. (A15), we have used the relation

$$f_i^{(\lambda)}=\sum_{j} \tilde{M}_{ij}^{(\lambda)} c_j^{(\lambda)}. \tag{A16}$$

In principle, Eq. (A15) must be solved for each of the four eigenvalues of $C_4$. However, as we mentioned above, if we are only interested in the FIR-active modes of the system, we can project into the invariant subspace of $\Gamma_5$, and only have to consider at most, $\lambda^{(3)}$ and $\lambda^{(4)}$. This can be made more transparent as follows. The reciprocal lattice vector $\mathbf{G}_{i\alpha}$ is given by (see Fig. 6)

$$\mathbf{G}_{i\alpha}=|G_{i1}|[\cos(\phi_{i\alpha}),\sin(\phi_{i\alpha})], \tag{A17}$$

where

$$\phi_{i\alpha}=\theta_i+\frac{(\alpha-1)\pi}{2}, \tag{A18}$$

and

$$\theta_i\equiv\cos^{-1}\left(\frac{G_{i1,x}}{|G_{i1}|}\right). \tag{A19}$$

The inhomogeneous vector on the right-hand side of Eq. (A15) is determined from Eq. (A12). Using Eq. (A17) in Eq. (45), we obtain the expression $b_{i\alpha}$

$$b_{i\alpha}=-E_0[i\tilde{\omega}\cos(\phi_{i\alpha})-\omega_c\sin(\phi_{i\alpha})]|G_{i1}|\psi_0[\mathbf{G}_{i1}], \tag{A20}$$

which yields

$$b_i^{(\lambda=1)}=0$$

$$b_i^{(\lambda=-1)}=0 \tag{A21}$$

$$b_i^{(\lambda=i)}=-i|G_{i1}|\psi_0[\mathbf{G}_{i1}]E_0(\tilde{\omega}+\omega_c)e^{i\theta_i}$$

$$b_i^{(\lambda=-i)}=-i|G_{i1}|\psi_0[\mathbf{G}_{i1}]E_0(\tilde{\omega}-\omega_c)e^{-i\theta_i}=b_i^{(\lambda=i)\star}(-\omega).$$

Therefore, as expected, we only require the $\lambda=\pm i$ eigenvalues to fully describe the FIR response. In particular, the determination of the power absorption is reduced to a solution of Eq. (A15) for $\lambda=\pm i$. Using these solutions in Eq. (43), we finally obtain the following explicit expression of the power absorption:

$$\frac{\langle P\rangle_t}{A}=\frac{1}{2}E_0\,\mathrm{Re}\left[\frac{i\tilde{\omega}n_0[\mathbf{G}=0]E_0}{\tilde{\omega}^2-\omega_c^2} - \frac{4}{\tilde{\omega}-\omega_c}\sum_i |G_{i1}|\psi_0[\mathbf{G}_{i1}]\sum_j \tilde{M}_{ij}^{(\lambda=i)}c_j^{(\lambda=i)}e^{-i\theta_i} - \frac{4}{\tilde{\omega}+\omega_c}\sum_i |G_{i1}|\psi_0[\mathbf{G}_{i1}]\sum_j \tilde{M}_{ij}^{(\lambda=-i)}c_j^{(\lambda=-i)}e^{i\theta_i}\right]. \tag{A22}$$

To obtain the normal mode frequencies, we use the homogeneous version of Eq. (A15) with $\gamma=0$. In this case, all *positive* eigenvalues for $\lambda=\pm i$ can be obtained from the full set of eigenvalues for $\lambda=i$. The negative eigenvalues simply correspond to the positive eigenvalues for $\lambda=-i$. This is the method used to generate the magnetic dispersion of the FIR-active modes shown in Figs. 2, 4, and 5.

[1] U. Mackens, D. Heitmann, L. Prager, and J. P. Kotthaus, Phys. Rev. Lett. **53**, 1485 (1984).
[2] D. Heitmann and J. P. Kotthaus, Phys. Today **46** (6), 56 (1993).
[3] J. H. Davies, *The Physics of Low-Dimensional Semiconductors: An Introduction* (Cambridge University Press, Cambridge, England, 1997).
[4] T. Demel, D. Heitmann, P. Grambow, and K. Ploog, Phys. Rev. Lett. **64**, 788 (1990).
[5] T. Demel, D. Heitmann, P. Grambow, and K. Ploog, in *Sixth International Winterschool on Localization and Confinement of Electrons in Semiconductors*, edited by G. Bauer, H. Heinrich, and F. Kuchar (Springer, Berlin, 1990).
[6] S. S. Nazin and V. B. Shikin, Fiz. Nizk. Temp. **15**, 227 (1989) [Sov. J. Low Temp. Phys. **15**, 127 (1989)].
[7] P. A. Maksym and T. Chakraborty, Phys. Rev. Lett. **65**, 108 (1990).
[8] V. Shikin, S. Nazin, D. Heitmann, and T. Demel, Phys. Rev. B **43**, 11 903 (1991).
[9] V. Gudmundsson and R. Gerhardts, Phys. Rev. B **43**, 12 098 (1991).
[10] D. Pfannkuche and R. Gerhardts, Phys. Rev. B **44**, 13 132 (1991).
[11] S. Nazin, K. Tevosyan, and V. Shikin, Surf. Sci. **263**, 351 (1992).
[12] Z. L. Ye and E. Zaremba, Phys. Rev. B **50**, 17 217 (1994).
[13] E. Zaremba and H. C. Tso, Phys. Rev. B **49**, 8147 (1994).
[14] E. Zaremba, Phys. Rev. B **53**, R10 512 (1996).
[15] A. L. Fetter, Ann. Phys. (N.Y.) **88**, 1 (1974); A. Eguiluz and J. J. Quinn, Phys. Rev. B **14**, 1347 (1976); S. Das Sarma and J. J. Quinn, *ibid.* Phys. Rev. B **20**, 4872 (1979).
[16] G. Eliasson, P. Hawrylak, J.-W. Wu, and J. J. Quinn, Solid State Commun. **60**, 3 (1986).
[17] G. Eliasson, J.-W. Wu, P. Hawrylak, and J. J. Quinn, Solid State Commun. **60**, 41 (1986).
[18] W. Y. Lai, A. Kobayashi, and S. Das Sarma, Phys. Rev. B **34**, 7380 (1986).
[19] V. Cataudella and V. M. Ramaglia, Phys. Rev. B **38**, 1828 (1988).
[20] C. A. Ullrich and G. Vignale, Phys. Rev. B (to be published).
[21] O. Magnúsdóttir and V. Gudmundsson, Phys. Rev. B (to be published).
[22] B. P. van Zyl and E. Zaremba, Physica E (to be published).
[23] B. P. van Zyl and E. Zaremba, Phys. Rev. B **59**, 2079 (1999).
[24] For a review, see W. Kohn and P. Vashishta, in *Theory of the Inhomogeneous Electron Gas*, edited by S. Lundqvist and N. H. March (Plenum, New York, 1983), p. 79.
[25] Strictly speaking, the von Weizsäcker correction vanishes identically for a weakly modulated 2DEG. It should therefore be viewed as a phenomenological term in our model which is chosen to have the form found in the 3D formalism. In this way, we retain the Schrödinger-like equation, viz., Eq. (3), for the determination of the density, thereby ensuring the expected quantum-mechanical behavior of the density in classically forbidden regions.
[26] In the $\mathbf{q}=0$ limit, the $\mathbf{G}''=0$ term of the Hartree matrix defined in Eq. (38) is singular. When this specific term is substituted into Eq. (37), we obtain the contribution $(4\pi/q)\,\psi_0[\mathbf{G}]\Sigma_{\mathbf{G}},\psi_0[-\mathbf{G}']c_{\mathbf{G}},$. The sum here is proportional to the *total* integrated induced charge in a unit cell, which vanishes for localized dots. Thus this problematic term makes no contribution and can be eliminated from the calculation.
[27] P. Bakshi, D. A. Broido, and K. Kempa, Phys. Rev. B **42**, 7416 (1990).
[28] D. A. Broido, K. Kempa, and P. Bakshi, Phys. Rev. B **42**, 11 400 (1990).
[29] J. Dempsey, N. F. Johnson, L. Brey, and B. I. Halperin, Phys. Rev. B **42**, 11 708 (1990).
[30] D. Huang and P. R. Antoniewicz, Phys. Rev. B **43**, 2169 (1991).
[31] D. Pfannkuche, V. Gudmundsson, P. Hawrylak, and R. R. Gerhardts, Solid-State Electron. **37**, 1221 (1994).
[32] M. Wagner, A. V. Chaplik, and U. Merkt, Phys. Rev. B **51**, 13 817 (1995).
[33] V. Gudmundsson, A. Brataas, P. Grambow, B. Meurer, T. Kurth, and D. Heitmann, Phys. Rev. B **51**, 17 744 (1995).
[34] E. Lipparini, N. Barberán, M. Barranco, M. Pi, and Ll. Serra, Phys. Rev. B **56**, 12 375 (1997).
[35] J. F. Dobson, Phys. Rev. Lett. **73**, 2244 (1994), and references therein.
[36] J. D. Jackson, *Classical Electrodynamics*, 2nd ed. (Wiley, New York, 1975).
[37] K. Kern, D. Heitmann, P. Grambow, Y. H. Zhang, and K. Ploog, Phys. Rev. Lett. **66**, 1618 (1991).
[38] Y. Zhao, D. C. Tsui, M. Santos, M. Shayegan, R. A. Ghanbari, D. A. Antoniadis, and H. I. Smith, Appl. Phys. Lett. **60**, 1510 (1992).
[39] For an introduction to point groups, see J. P. Elliot and P. G. Dawber, *Symmetry in Physics: Further Applications* (The MacMillan Press Ltd., London, 1979), Vol. 2.